

In-situ kinetic study of irradiation induced crystallization in amorphous Al₂O₃

D. Loiacono^{a,b,d}, M. Vanazzi^a, B. Paladino^a, W.-Y. Chen^c, M. Cabrioli^{a,b}, M. Li^c, M.G. Beghi^b, F. Di Fonzo^{a,d,*}

^a Center for Nano Science and Technology @PoliMi, Istituto Italiano di Tecnologia, Via Pascoli 70/3, 20133, Milano, Italy

^b Energy Department, Politecnico di Milano, Via Ponzio 34/3, 20133, Milano, Italy

^c Nuclear Science and Engineering Division, Argonne National Laboratory, 9700 S. Cass Avenue, 60439, Lemont, IL, USA

^d X-nano S.r.l, Via Rubattino 81, 20134 Milano, Italy

ARTICLE INFO

Keywords:

Nuclear materials

Ceramic coatings

Radiation induced crystallization

ABSTRACT

In the last ten years amorphous alumina coatings, deposited by Pulsed Laser Deposition, emerged as potential key enabling technology in the fields of heavy liquid metal fast reactors (lead and lead-bismuth) and fusion. In the former, as coating of the steel fuel cladding and in the latter as multifunctional coating providing a barrier against tritium permeation, steel corrosion and electrical insulation. Nevertheless, a detailed knowledge of the behavior of this thermodynamically metastable material at high temperatures and under neutron irradiation is still unknown. A knowledge gap that is mandatory to fill up for the deployment of this barrier technology. In the present work, we present a first step towards this goal, by the in-situ dynamic observation of the radiation induced crystallization processes of thin films of amorphous Al₂O₃, induced by ion-irradiation over an extensive range of temperatures (400–800 °C). The study was performed at the Intermediate Voltage Electron Microscope (IVEM)-Tandem Facility at Argonne National Laboratory. The experimental findings allow to elucidate the dependence of the grain growth on ion dose and temperature. A kinetic approach has been used to derive the process activation energies and other important parameters.

1. Introduction

The strive for higher thermodynamic efficiency in new power generation technologies often implies much harsher conditions than those encountered in established heat cycles based on fossil or nuclear fuels. In the latter, in particular, lead and molten salt cooled fast reactors, the front runners of the generation IV fission nuclear technology (GEN IV), pose unprecedented requirements on material performances with operating temperatures close or even higher than 800 °C [1] in direct contact with highly corrosive working fluids and end-of-life radiation doses higher than a hundred displacements per atoms (dpa). Similar requirements are met also for the breeding blanket of fusion power reactors where tritium permeation is the main engineering challenge, even more so than corrosion or radiation damage [2].

In this context, amorphous oxide coatings deposited by Pulsed Laser Deposition on austenitic and martensitic steels emerged in recent years as a key enabling technology for heavy liquid metal (HLM) cooled fast

reactors and fusion power plants, due to their unique ability to concurrently solve the issues of corrosion of structural steels, erosion, tritium permeation and electrical coupling between coolant and the metallic structures [3–9]. Besides these functional properties, these hard, fully dense and compact ceramic barriers turn out to achieve an unusual ensemble of metal-like mechanical properties, superior plastic behavior and wear resistance, as well as strong interfacial bonding [3–8].

In particular, PLD-grown Al₂O₃ coatings have a peculiar combination of all these features, making them a promising candidate for protecting steels from corrosion in HLM systems at high temperatures. Furthermore, because of these outstanding physico-chemical properties, PLD deposited amorphous Al₂O₃ (a-Al₂O₃) could find applications in several other industrial domains. The main question that remains unanswered about this material is its behavior under neutron irradiation. Even though efforts are being undertaken in order to gather data on neutron irradiation of PLD deposited amorphous Al₂O₃, its high cost and

* Corresponding author.

E-mail address: fabio.difonzo@iit.it (F. Di Fonzo).

<https://doi.org/10.1016/j.jnucmat.2023.154805>

Received 31 December 2022; Received in revised form 24 September 2023; Accepted 29 October 2023

Available online 4 November 2023

0022-3115/© 2023 The Authors. Published by Elsevier B.V. This is an open access article under the CC BY license (<http://creativecommons.org/licenses/by/4.0/>).

complexity make it a long-term task. In the near term, ion irradiation can be a useful tool for preliminary studies. Since several years, heavy ion irradiation has emerged as an effective emulating tool to investigate the materials behavior under neutron irradiation. Ion irradiation avoids the complexities of in reactor testing, and allows to achieve high damage rates with negligible or no residual radioactivity. Ion irradiation thus allows substantially shorter irradiation campaigns (including irradiation and post-irradiation analysis), at a significantly lower cost. It has therefore become an invaluable tool for understanding and predicting neutron damage in materials [10]. Beside this, it is recognized to be a unique tool to produce controlled defects, structural disorder, stress, phase transformations, and, in general, to modify the physical properties of materials [11].

Nevertheless, the differences between neutrons and heavy ions must be considered to design a proper experiment with the latter representative of the former. While neutrons lose energy only through discrete collisions with the material's nuclei, energetic ions, on their passage through matter, suffer depth-dependent energy losses due to both the collisions with the target nuclei and the collisions with the target electrons. Due to the high number of electrons and to their small mass, the latter energy losses have a more continuum character. These losses, termed respectively nuclear (S_n) and electronic energy (S_e) losses, characterize the interaction modes between incident ions and the exposed material. In particular, the ratio S_e/S_n - called Electronic to Nuclear Stopping Power (ENSP) ratio - is a crucial parameter to compare the effects of charged particles (from electrons to heavy ions) to those induced by neutrons [12].

Moreover, in the case of neutron irradiation the term S_e is not null (and therefore also the ENSP ratio is not null), because, while a direct transfer of energy from neutrons to electrons is absent, the atoms displaced by the collisions of neutrons (the knocked-on atoms in a collisional cascade) do interact with electrons, thus transferring some energy to them. Nuclear and electronic energy losses depend mainly on the energy and mass of the accelerated ions. The ENSP ratio generally increases with increasing energy, while it is reduced by increasing the ion mass [13]. Broadly speaking, in metals and alloys with metallic bonding involving delocalized electrons, the energy deposited to target electrons is more rapidly dissipated, resulting mainly in a local heating of the material without structural transformations. Instead, in materials with covalent/ionic bonding involving predominantly well localized electrons, ionization effects are expected to be more significant, up to inducing artefacts due to electrostatic interactions [14–16].

Anyhow, it is commonly accepted that higher values of the S_e/S_n ratio tend to slow down damage accumulation, because a higher fraction of energy which is released to electrons means a higher fraction of energy available for local heating (thermal spike), promoting annealing and recovery processes along the ion trajectory [15,16].

Based on the available literature, a comprehensive understanding of the impact of electronic and nuclear energy losses on glassy amorphous ceramics, specifically the class of material studied in this paper, does not exist. As a consequence, the authors have opted to employ the available data pertaining to crystalline ceramics and crystalline alumina as an initial reference. It is important to note that this approach may not be entirely appropriate for amorphous materials such as a- Al_2O_3 . Further adjustments may be necessary as more knowledge is gained in this area.

Previous studies have investigated the material-dependent effects of electronic energy losses on ceramic crystalline materials, namely [12,17,18]. These investigations have revealed that combining nuclear and electronic energy losses can substantially reduce accumulated damage. Thomè et al. have demonstrated that this “healing effect” may occur in specific ceramic crystalline materials when the S_e outweighs the S_n and is determined on the balance between defects creation and annihilation. This balance depends, on one side, on the physicochemical properties of the irradiated material, and on the other side on the irradiation conditions: temperature, low/high energy ion fluences, and dose rates [12,17,18].

Zinkle et al. [13] reported the theoretically appropriate ENSPs for systems characterized by a fast neutronic spectrum, such as fast breeder and fusion reactors, indicating values below 13 as the correct range. The value for ENSP suggested in [13] is based on the impact of ionization-enhanced migration of oxygen vacancies on the development of dislocation loops in Al_2O_3 crystals. This resulted from the observations that the dependence on the irradiation spectrum observed may carry important implications [19]. Specifically, light ions irradiation, such as protons and electrons, having ENSP ratios exceeding 1000, are unsuitable for simulating ceramics' behavior under typical fission or fusion neutron irradiation conditions. An ENSP ratio of approximately 10 could be more convenient [19].

Anyhow, since the interplay between all of these mentioned effects on a- Al_2O_3 has not been elucidated yet, based on the available knowledge, it is considered a good practice to minimize the ENSP ratio in the experimental design of ion irradiation experiments.

Previously, the behavior of amorphous a- Al_2O_3 films deposited by PLD on steel has been studied under irradiation by 12 MeV Au^{5+} and 18 MeV W^{8+} at 600 °C, up to 150 dpa [20], and under Ni [21] and Au [9] irradiation at room temperature, with ex-situ post-irradiation analyses. The general picture which emerges from these studies is a temperature dependent response to irradiation, with no major modification occurring at room temperature, whilst, at 600 °C, a general trend towards the formation of nanocrystals. In particular, in all the studied conditions, nanocrystals with mean size growing with dpa in a sublinear way have been observed. Some effect of the ion used has been observed as a second order effect on the growth kinetics [21].

Different crystalline phases nucleates, depending on the irradiation conditions and no failure is observed despite the change in structure [21]. Mechanically, the process of radiation-induced crystallization (RIC) caused an increase in the hardness and stiffness compared to the pristine material. Still, the irradiated films did not become fragile. Nano-indentation and nano-scratch tests - repeated after ion irradiation - showed a certain level of plasticity left in the system [20,4]. Thanks to these studies, the general trends are clear, but a complete kinetic picture of the RIC in amorphous Al_2O_3 films is still missing.

The present study aims at filling this gap by ion beam irradiations with in situ TEM observation, at various temperatures. In this way we reached a comprehensive understanding of the synergistic effects of ion irradiation and temperature on the structural evolution of the amorphous alumina, which cannot be probed through traditional post-irradiation examination.

2. Materials and methods

2.1. Sample preparation

The fabrication of the alumina samples was performed employing a PLD set up improved over the configuration already used to coat large area samples. Depositions were carried out in a custom steel vacuum chamber at room temperature. After reaching a base pressure of 10^{-3} Pa, oxygen gas was injected into the chamber so to maintain a constant pressure of 0.15 Pa. A pulsed laser in the U.V. (Coherent® COMPex 205F, wavelength 248 nm, 20 ns pulse duration) is operated at 20 Hz, with an energy fluence on target of 3.5 J/cm^2 . The laser ablates a polycrystalline pure (99.99%) Al_2O_3 (Testbourne Ltd Company®). Further details about the deposition set up can be found elsewhere [5,22].

Films with nominal thicknesses of 100 nm were grown on monocrystalline substrates obtained by cleaving a NaCl crystal. After deposition, each sample was put in warm distilled water, where the salt dissolved and the oxide film floated on the water's surface. TEM grids were used to pick up the films, to be ready for analysis in the TEM. Additional information about this floating technique is included in [7].

The thickness limit of 100 nm was selected to steer clear of the spatial resolution degradation in TEM resulting from an augmented number of inelastically scattered electrons due to the increased thickness, as well as

to prevent any surface effects that may be induced by lower thicknesses. Samples tested at temperatures below 600 °C were laid on PELCO® 2000 mesh Cu grids from Ted Pella, Inc. To perform the irradiation tests at temperatures above 600 °C, ceramic Si₃N₄ membranes and Molybdenum grids (PELCO® from Ted Pella, Inc.) are used to pick and support the floating films.

2.2. Irradiation experiments

The in situ irradiation experiments were carried out in the IVEM facility. It includes an intermediate voltage transmission electron microscope and an ion implanter. The combination of these instruments offers a unique capability for a wide range of in situ experiments involving ion irradiation or ion implantation with simultaneous transmission electron microscopy. More information about the IVEM facility is covered in [23].

The PLD deposited alumina films were subjected to thermal heating until stabilization thermal equilibrium at different temperatures (400, 500, 600, 700, 800 °C), then irradiated with an ion flux of $6.25 \cdot 10^{11}$ ions/cm²s. Fluences required for reaching 1 dpa were $8.5 \cdot 10^{14}$ ions / cm². For each experiment, the ion flux was measured to an accuracy of $\pm 10\%$ by an annular Faraday cup located within the microscope at 4 cm from the sample [23].

The above choices were based on simulations performed by the SRIM code [24]. The main outcomes, such as implantation profile, ENSP ratio and damage events, are summarized in different plots in the supporting information section (Figure 12 and Figure 13). In the present work, the values exploited for displacements threshold energies for Al₂O₃ are the ones given by default by SRIM: 25 eV for Al and 28 eV for O. It is worth remembering that these values are averages of direction dependent values [25].

While the ion implantation depth does not differ significantly when computed by the "Ion Distribution and Quick Calculation of Damage - cascades" mode or the "Full Cascade Damage" mode, it is not the same for the damage production. Several papers discuss this discrepancy quantitatively. Moreover, the outcomes of these simulations crucially depend on the adopted values for the threshold energies for displacements. We note that the scientific community is still debating the best approach for evaluating dpa based on SRIM simulation [26–29], as multiple papers suggest slightly different procedures. The Norgett, Robison, Torrens (NRT) standard [29], despite some limitations, is the industry standard for calculating dpa in all reactor Monte Carlo codes. It is a simple and general form suitable for analytical calculations and computer code implementations, although it was originally developed for mono-elemental materials [29]. The "quick damage" SRIM simulation option is preferred for comparing with reactor radiation dpa data since its results conform most closely to the "NRT standard dpa" prescribed by simulation studies [29]. The use of other options could deviate from the defined standard.

It has also been suggested to adopt the SRIM "Quick calculation" option as a backup alternative, when calculating the effective damage energies for compounds is impossible or when the user wants to avoid manual manipulation of SRIM data files [28]. However, The authors in [28] acknowledge that moderate quantitative errors may arise, with a maximum calculated vacancy production error of around 30% [28].

It is important to emphasize that the dpa value alone is usually insufficient to describe ceramic ion irradiation effects. Most energy lost by heavy ions could be transferred to the lattice electrons, producing ionization. Ionizing effects are more pronounced in ceramics than in metals, and these effects need to be considered when comparing results obtained in different irradiation environments in ceramic experiments. The ENSP ratio discussed above appears to be a valuable additional parameter for evaluating irradiation spectrum effects in ceramics, as discussed in [13]. The ENSP values, calculated by SRIM, were below 1.5 throughout the whole film thickness, as presented in the Figure 12 reported in the supporting information section.

3. Results

Direct observation of the films under irradiation revealed the ion irradiation-induced particle nucleation and then their growth, as it can be observed in Fig. 1. Crystallite growth occurred for all irradiation temperatures examined, even below 600 °C, which is the boundary temperature below which thermally induced crystallization does not occur in PLD Al₂O₃, as reported in [20], where no discernible crystallization or grain growth are found during annealing for 90 min at 600 °C. The evolution of the microstructure was followed by sequentially taking bright-field images (BF), dark field images (DF) and diffraction patterns (SAED) of the films while they were being irradiated.

3.1. Irradiation induced nucleation and phase evolution

During the various in-situ irradiation experiments SAED patterns were recorded to precisely identify the onset of crystallization (Fig. 2). In each pattern, rings dimensions were measured, determining the crystalline phases present in the system by a direct comparison between the interplanar distances (d-spacings) obtained and the databases present in literature [30,31].

The phase recognition was not straightforward because each pattern consists of an overlapping signal from grains of different phases. Indeed, alumina has an abundant number of metastable transition phases that appear before the only stable α -phase as discussed in [32], and at least for the thermally induced crystallization, the phase transformations are strongly related to the deposition method and temperature [33]. Furthermore, the different crystalline planes often present d-spacings very close to each other, making a unique attribution to one of the possible crystalline structures sometimes impossible. Apart from the principal γ -Al₂O₃ directions, which produce in any experiment the brightest reflections, several other contributions (Table 1) have been detected: according to database, θ -Al₂O₃ or δ -Al₂O₃ meta-stable phases [30,31].

To have a more precise representation of the evolution, SAEDs were also analyzed by a rotational average procedure, using the DiffTools script in DigitalMicrograph™ [34]: the two-dimensional SAED patterns are rotationally averaged about a chosen center, obtaining a one dimensional intensity profile, in reciprocal space, as shown in Fig. 3. The peaks corresponding to the different phases are thus better identified; these one dimensional profiles will be called SAED diffraction patterns. Furthermore, the Fig. 3 is a valuable tool for visually demonstrating the impact of temperature on the nucleation of particles and the resulting phase transformations in the material induced by ion irradiation. Notably, the identification and classification of these distinct phases are detailed in the Table 1.

As reported above, alumina has several phases with d-spacings very close to each other, hence a unique attribution to different phases is difficult. This problem was overcome thanks to the availability of an extensive set of XRD diffractograms, obtained in a previous study which investigated the thermal crystallization of alumina samples deposited by PLD. Exploiting Bragg's law in the form:

$$Q[nm^{-1}] = \frac{4\pi}{\lambda} \sin\left(\frac{2\theta}{2}\right) \quad (1)$$

where Q is the wavevector in the reciprocal space, λ is the working wavelength of the diffractometer and 2θ is the diffraction angle. Each XRD diffractogram was converted into the form of a one dimensional intensity profile in reciprocal space, i.e. the same form of the SAED patterns. After the conversion, being both the diffractograms (SAED and XRD) in the same form, a direct comparison can be done, as shown in Fig. 4. A perfect overlap is found between the peaks in the RIC and in the thermally induced one, allowing to achieve a more reliable identification of phases in the irradiated samples. Phases attribution is presented in the Discussion section.

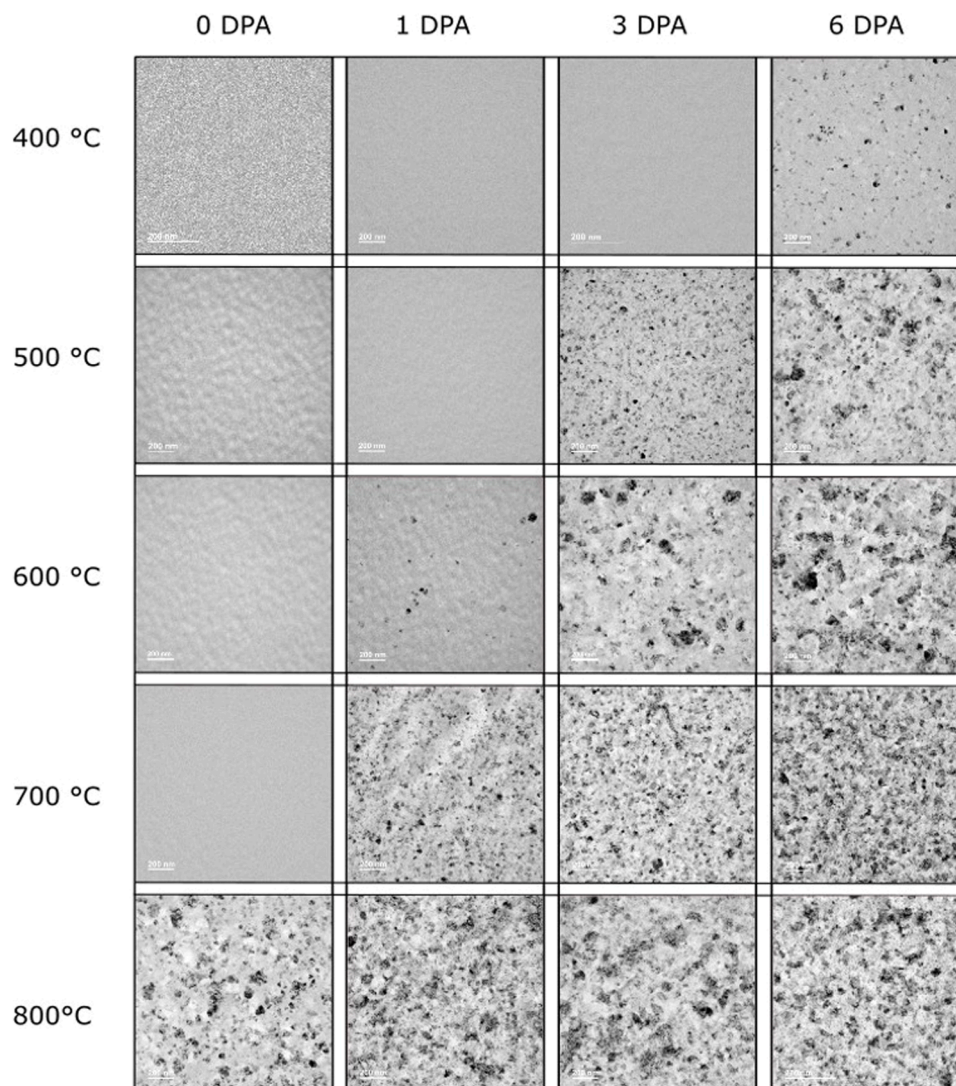


Fig. 1. Bright field images of the radiation induced crystallization in Al_2O_3 film at different temperatures.

3.2. Crystallite growth kinetics

The average crystallite size evolution was studied, measuring it from DF (Fig. 5) at the different fluences for the first appearing reflection in SAED. This is related to the [440] plane of the γ polymorph.

For each micrograph, from 15 to 130 particles were analyzed, and the area of each particle was measured through the open-source program ImageJ [35]. The variability in the number of particles analyzed depends on two factors: in low dose micrographs, few particles were present, while at high dpa values, due to the overlapping of different particles, only the discernible, not-overlapped, single particles were analyzed.

The Fig. 6 summarizes the DF images, highlighting the initial dose at which radiation-induced nucleation occurred for each temperature analyzed. It is important to note the effect of temperature on the number and size of particles nucleated. At temperatures below the crystallization temperature of alumina (i.e., 600 °C), a consistent and nearly uniform number of particles (typically ranging between 15 and 30 particles) is observed. Conversely, at higher temperatures, more particles are detected, even at the lowest dpa value analyzed. Remarkably, in the latter case, the number of recognizable particles consistently exceeded 100, and the size of particles at 800 °C was observed to be even bigger than other temperatures.

Describing the effect of particle density with increasing doses is more

complex. While at temperatures lower than the crystallization temperature, the nucleation of particles increases with the dose, as evident from Fig. 1 for the specific case of 600 °C. However, at 700 °C and 800 °C temperatures, it is difficult to determine whether the initially nucleated particles are growing solely or if there is concurrent nucleation occurs. This is due to the uniform crystallized region and the fact that images at progressively higher doses analyze different regions of the material and are, therefore, uncorrelated.

The average crystallite size was then plotted versus ion dose for the different irradiation temperatures. As discussed above, to compare the crystallite growth kinetics between different materials, the dpa is the most helpful parameter. Hence, although the data are plotted as a function of both dpa and fluence, the fitting procedure, discussed later, is done with dpa values.

It is worth underlining that each point is plotted with its corresponding Standard Error of the Mean (SEoM) as error bar. The SEoM is the standard deviation σ divided by the number of elements of the statistical population. It represents the precision of the value of the mean, rather than the dispersion of particle sizes. Indeed, as it can be easily understood, the standard deviation of the crystallite dimension grows as the dose increases, also because, at a high dose level, new crystallites nucleate while the older ones continue to grow.

The crystallization kinetic models for different classes of materials have been discussed in detail [36–39]. In one of the first proposed

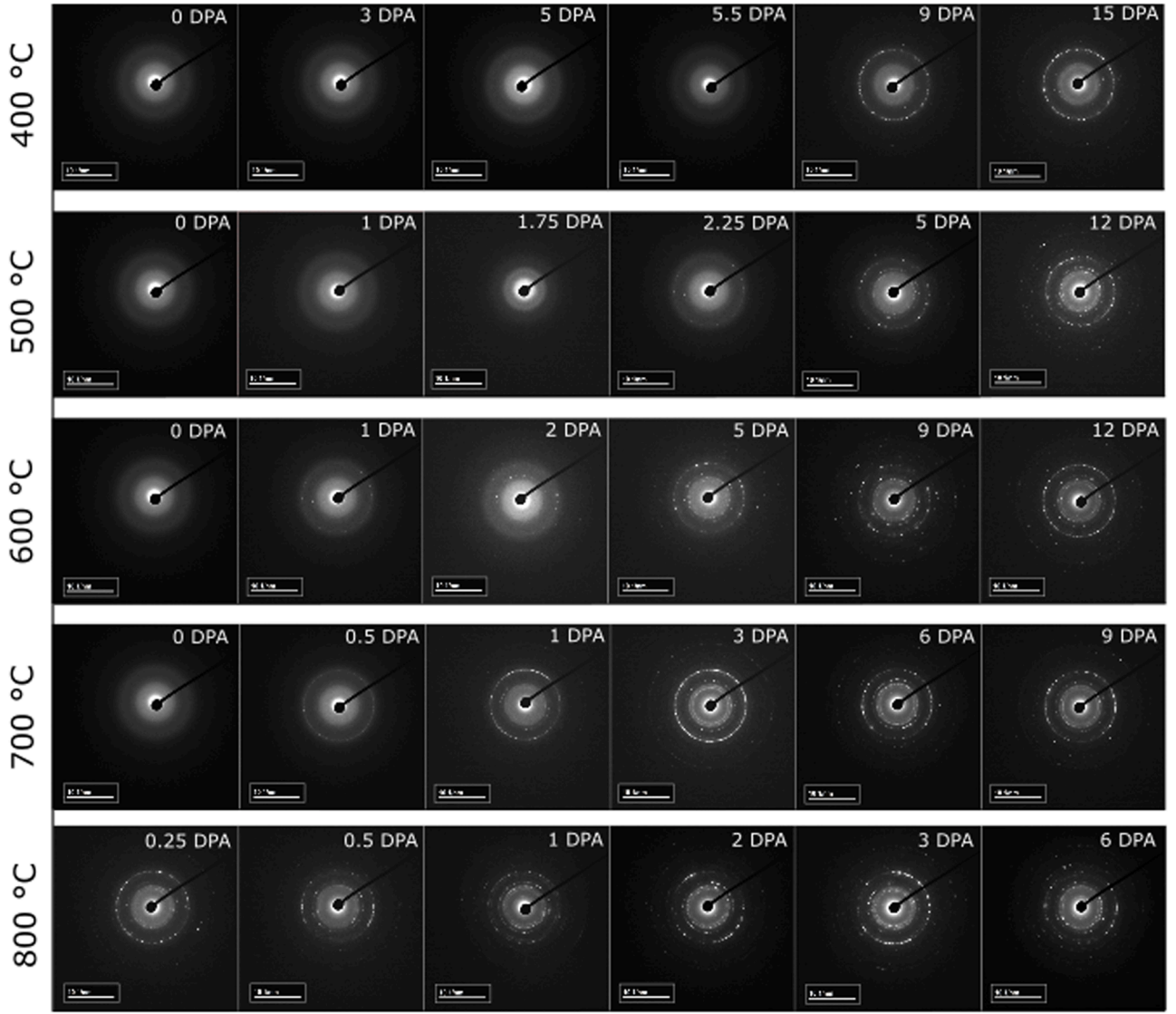


Fig. 2. Radiation-induced crystallization diffraction pattern evolution in Al_2O_3 films at different temperatures.

Table 1
Phase appearance evolution at different temperatures.

Order of appearance	d-spacing	phases attributed	Temperature of appearance
1	1.438 ± 0.0053	γ [440]	400, 500, 600, 700, 800
2	2.034 ± 0.0028	γ [400]	400, 500, 600, 700, 800
3	2.884 ± 0.001	δ / θ [401]	500, 600, 700, 800
4	2.46 ± 0.0024	θ [111] / δ [312]	500, 600, 700, 800

models, Burke and Turnbull [37] deduced a parabolic relationship for the thermally induced grain growth kinetics:

$$D_g^2 - D_0^2 = kt \quad (2)$$

Where D_0 is the initial grain size, k is the proportionality constant that depends on absolute temperature and activation energy, t is holding time at a steady temperature T . For the proportionality constant k of a temperature dependence of the Arrhenius type is proposed:

$$k = k_0 e^{-\frac{E_a}{RT}} \quad (3)$$

where E_a is the activation energy for grain growth, k_0 is the total pre-exponential constant and R is the gas constant.

The relation of Eq. (2) turns out to accurately describe the experimentally observed behaviors only in limited sets of cases. Mechanisms can be active, which slow down the kinetics of grain growth. In order to represent these cases, a generalization of Eq. (2) has been proposed [40].

$$D_g^n - D_0^n = kt \quad (4)$$

where the exponent 2 is substituted by other values. Values of n between 2 and 5 have been reported for various metallic systems [41–43]. Grain growth kinetics have been extensively measured also in ceramics, and the data reveal a similar range of grain growth exponents [44–47].

Most of the investigators tried to explain the exponents in terms of the parabolic grain-growth kinetics ($n = 2$) and of phenomena that can explain the deviation from this value. In the literature [37,48], different n dependences from external stress, recrystallization path and grain shapes have been reported. In [49] the possible relationships between n and the crystallization temperature and materials purity have been investigated, without finding general trends. It is worth mentioning that

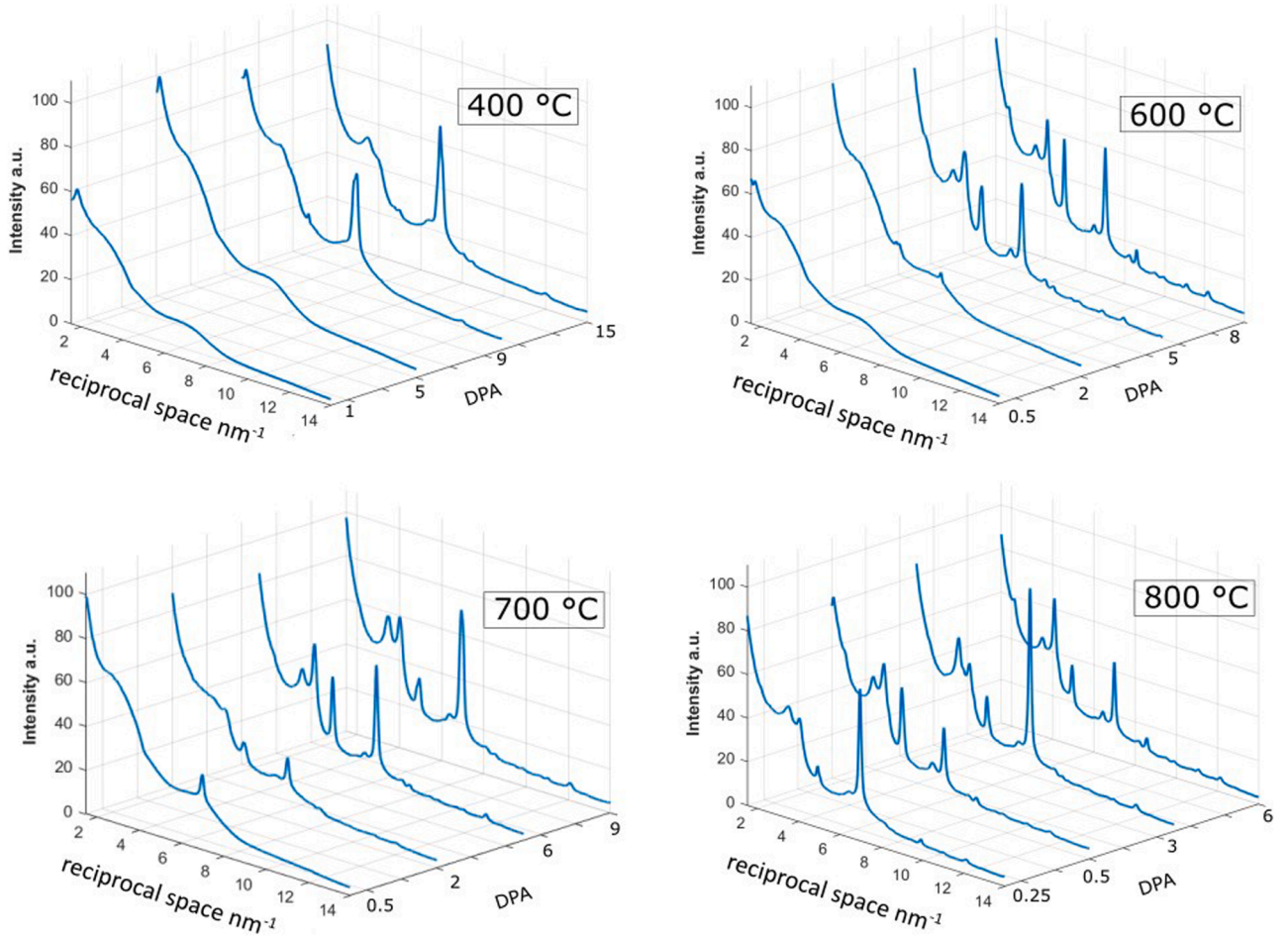


Fig. 3. Diffraction patterns in reciprocal space, obtained from an intensity profile extraction from SAEDs. The appearance of different peaks highlights the phase evolution at different temperatures.

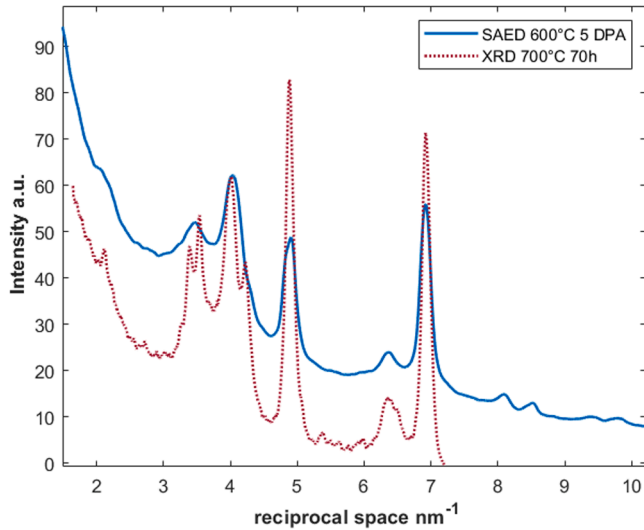


Fig. 4. SAED diffraction patterns in reciprocal space, [600 °C 5 dpa] and XRD pattern annealed sample [70 h 700 °C] in reciprocal space compared.

in Eqs. (3) and (4) both n and E_a are considered constant during the transformation process [50].

When the grain growth process occurs under irradiation, a modified version of Eq. (4) can be derived [51]. Grain size increases with the ion

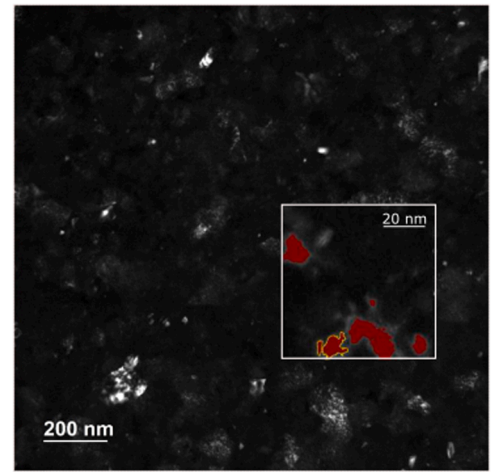


Fig. 5. Dark field picture with a magnification of a specific region of the image where the crystallite selection process is highlighted.

fluence (φ) (when the ion flux is constant $\Phi = \varphi/t$) according to an analogous power law relation

$$D_g^n - D_0^n = k_{irr}\varphi = k_{irr}\Phi t \quad (5)$$

where n and t have the same meaning of Eq. (4), and k_{irr} is the kinetic constant for the irradiation induced process, which depends on the

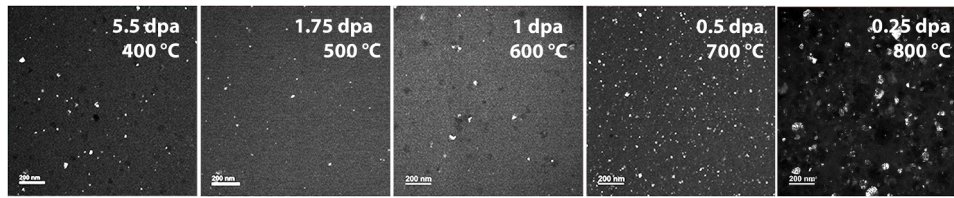


Fig. 6. The DF images show the temperature's impact on nucleation. The number of particle nucleated increases when temperature is higher than crystallization temperature.

materials properties and the irradiation conditions.

The Eq. (5) can be further modified in order to express the evolution as a function of the dpa value:

$$D_g^n - D_0^n = K \cdot dpa \quad (6)$$

For the k_{irr} and K kinetic constants, the same Arrhenius form of Eq. (3) is assumed.

Kaoumi et al. [52] could analytically extrapolate the Eq. (5) with an exponent equal to 3 using the concepts of radiation-enhanced diffusion, rate theory, and the thermal spike hypothesis. Kaoumi et al. [52] developed this grain growth model under ion irradiation based on the impact of thermal spikes induced by irradiation on the grain boundaries. In these conditions, grain growth occurs thanks to the enhanced radiation diffusion and the local driving force of the grain boundary curvature. The same model can also explain the grain growth in the so-called thermally assisted regime. Furthermore, by analyzing the self-diffusion constant under atomic displacement environments, a different paper [53] elucidates how the growth of grains accelerates as a result of the combined impacts of temperature and radiation.

Before proceeding with the further presentation of the result, it is essential to address a specific point. This study focuses on the nucleation and subsequent growth of crystallite particles. So far, a general equation for irradiation induced particle growth in an amorphous material, does not exist. The Eqs. (5) and 6 presented above were derived based on crystalline materials and considering the diffusion rate of atoms and defects that lead to their interactions with the existing grain boundaries. Therefore these equations cannot be considered valid to describe the growth of crystallite particles nucleated in an amorphous material.

Considering the fact that in a crystalline material, the grain growth is well described by a sublinear correlation with the fluence and, hence of dpa; and given the clear evidence of an incubation dose prior particle nucleation (at temperatures lower than the crystallization temperature), a semi-empirical model is formulated to characterize the crystallite growth:

$$D_g^n = K \cdot (dpa - dpa_0) \quad (7)$$

Regarding the previous Eq. (6), in this case, the initial grain dimension D_0 has been assigned a value of zero since the material is initially amorphous and lacks crystals. K_a denotes the updated kinetic constant for the amorphous material, and the same Arrhenius form of Eq. (3) is assumed. While dpa_0 is the incubation dose required before the onset of radiation-induced crystallization.

In Fig. 7, the average nucleated particle sizes are plotted vs. the dpa values, for each irradiation temperature. A fitting procedure, performed by a Matlab script, allows to determine k_a , n and dpa_0 . The parameter dpa_0 has been established as a fitting parameter since the dpa values at which the first picture of the crystallized material was captured represents a progressed stage, and may not necessarily correspond to the dpa_0 value at which nucleation begins. Then by the Arrhenius equation (Eq. (3)) the activation energies and the k_0 prefactors are obtained. A deeper discussion about fitting and parater extrapolation is reported below, in the Discussion section.

3.3. Bright field images analysis

Since the outstanding properties of PLD alumina can be related to its peculiar amorphous/nano- crystalline microstructure, understanding how the amorphous fraction (AF) in the system evolves through the RIC is fundamental. For this reason, a procedure has been developed in order to obtain qualitative trends in AF at different temperatures. BF images were used to achieve this goal.

In BF images the amorphous region turns out to be brighter. Therefore, an average value of brightness is evaluated for the AF, then the appreciably darker parts are attributed to the crystalline component area fraction, and the AF is calculated from each image.

It should be pointed out that some criticalities are present in this procedure. In order to reduce them, for each value of dose, BF images are taken from three different angles in random areas, as discussed below. However, the outcome should be considered only a first order analysis.

Firstly in BF, the crystalline part far from the Bragg condition has a low diffraction contrast, and it would have similar brightness as the amorphous part. Moreover, as the dose increases and the amorphous fraction decreases, it becomes more challenging to determine the standard brightness for the amorphous part, and errors can occur in opposite directions. Either the brightest crystallite could be counted as amorphous, or the lower brightness amorphous parts counted as bright crystallite. For this reason, for each dose three BF images are taken from different orientations, and the results are averaged. Upon comparing the results obtained from various tilt measurements, it was observed that the standard deviation between the acquired values was approximately 10%. However, it is noteworthy that the observed standard deviation does not necessarily represent all the possible sources of measurement error. Whilst this procedure is to be perfected in order to be considered fully quantitative, yet it gives a coherent trend of the evolution of the amorphous fraction with dpa and temperature.

Another uncertainty comes from the fact that the nucleated particles are smaller than the film thickness, and the measured value of the crystalline transverse area fraction, from particle projection in BFs is larger than the actual volume fraction. For this reason, the particles projected area, measured in BFs, should have been converted in particle volume before making any evaluation of AF. Several statistical and experimental procedures to perform this conversion have been discussed [54,55]. However, due to the difficulties in their implementation and to the uncertainties which unavoidably affect the results, they have not been adopted because they could not introduce essential improvements.

The values obtained from the crystalline transverse area fraction are presented in the next section. In the light of the limitations highlighted above, the presented values of the fraction should be considered as affected by a limited accuracy. However, since they are all obtained by the same procedure, their differences, and therefore the resulting trends, should be more reliable than the absolute values. As a matter of fact, these fractions turn out to show meaningful trends.

4. Discussion

4.1. Irradiation induced crystallite nucleation and phase evolution

The results for different temperatures are reported in Fig. 3. A clear

dependence of the phases transformation on temperature is present, and several considerations can be made by direct observation. First, the temperature strongly determines the dose level at which RIC begin. For example, while at 400 °C the first hint of crystallization is visible at about 5.5 dpa, at 600 °C a similar hint is visible at 1 dpa, and, at 800 °C, at 0.25 dpa a substantial crystallization is already present.

The relation between the dpa for the onset crystallization and temperature is shown in Fig. 8. The relationship between these two parameters is well described by a power law with a negative exponent larger than 4. Due to this exponent, the extrapolation of this trend towards lower temperatures would suggest that at room temperature a practically infinite dose is required to induce crystallization. This is consistent with the recent observation of no crystallization hints even at 25 dpa at room temperature [9], and supports the indication of amorphous Alumina should be 'radiation tolerant coating'.

An important feature always present in each analyzed SAED, is connected to the central bright halo, visible in Fig. 2.

This contribution comes from the crystal lattice incoherence, highlighting that a complete crystallization did not occur in the system [56], also at high levels of dpa.

When the intensity profile is extracted, the halo is converted into a small hump grafted between 5 and 8 nm^{-1} . When the crystallization starts, the first reflection produces a peak growing from this hump, and with the crystallization progress, the hump progressively diminishes. Moreover, as the crystallization continues, the intensity of the γ -[400] peak, is gradually reduced, indicating that other phases (δ/θ) are growing in the system.

Regarding the phase recognition at different temperatures, the peak attributions, the order of appearance and the temperature at which they were present are reported for the primary reflections, in Table 1. However, several small other peaks are present, showing the complex structure present in the system Fig. 3.

Considering the 600 °C case, the crystallization started with the γ polymorph nucleation, showing a high-intensity reflection linked to the γ [400] plane. Increasing the dose to the system, other peaks appear. Different behaviors can be noticed at different temperatures. At 500 °C (and 700 °C), the phase evolution is essentially the same as the one described for 600 °C, being only slightly retarded (or accelerated) due to the lower (or higher) temperature. At 400 °C, instead, only the first two reflections reported in Table 1 were present also at the highest dpa level reached (15 dpa), and if compared with other cases, the crystallization starting dose was highly shifted. Indeed, in this case, a value of 5.5 dpa was needed for the RIC onset.

The evolution was further dissimilar at 800 °C, since the lowest dose analyzed (0.25 dpa). Moreover, a very complex pattern of reflections was present. At 0.25 dpa (Fig. 3), the diffraction intensity profile resembles the reflections that appeared at lower temperatures only at much higher values of dpa.

The other parameters (n and dpa_0) of the crystallite growth semi-empirical model in Eq. (7), obtained by fitting the experimental data, are presented in the Table 2 and further discussed in the 4.4 section.

The above considerations allow to perform a first distinction among three crystallization regimes: a high temperature one, which includes the 800 °C range, an intermediate temperature one, evident in the behaviors at 500, 600 and 700 °C, and a lower temperature one, visible at 400 °C.

Table 2
crystallite growth model parameters extracted from the fitting of the experimental points.

Temperature (°C)	n	dpa_0
400	3.7	3.9
500	4.9	1.63
600	6.2	0.98
700	6.8	0.45

The whole procedure described in the *Materials and Methods* section and summarized in Fig. 4, shows that the phase evolution of the radiation induced crystallization retraces exactly the same phase evolution induced by thermal crystallization. As discussed in [57] the PLD Al_2O_3 has the γ phase as the first appearing phase during the thermally induced crystallization, then passing through the δ/θ phases and reaching the only stable phase when temperature exceeds 1100 °C. The comparison between Fig. 2 and the evolution of thermal crystallization [57] confirms that irradiation has an accelerating effect in the crystallization process. Indeed the features observable for the case of thermal annealing at 700 °C for 70 h are the same that in the case of RIC are observable at 600 °C after a radiation dose of 5 dpa.

The similarity between the phase evolution of radiation-induced crystallization and thermally-induced crystallization at higher temperatures implies that thermal spikes, including both ballistic and electronic effects, may be more significant factors than displacement or atomic mobility in causing local temperature increases.

This finding could have important implications for understanding the mechanisms behind crystallization and could potentially lead to new methods for controlling the crystalline structure of materials. Further research is needed to elucidate the role of thermal spikes in radiation-induced crystallization fully and to explore their potential applications in science for these amorphous ceramic materials.

4.2. In-situ observation of ion-irradiation induced particle growth

As mentioned in Section 3.1, the ion induced particle growth kinetics was obtained from the analysis of the DF images at different fluences. A systematic analysis, in terms of the average crystallite size evolution, is presented here for the reflection due to the [440] plane of the γ polymorph. The experimental data and the curves obtained, at each temperature, by a best fit procedure for the behavior of Eq. (7) are reported in Fig. 7. The distinction, already emerging in the discussion of the SAED results, between the behaviors at higher (800 °C), lower (400 °C) and intermediate temperatures is confirmed.

A specific consideration has to be done for the 800 °C case in which a decreasing trend in the mean particle dimension appears at 1 dpa after a steep initial growth. Indeed, while all the other curves represent the best fit of Eq. (7), the behavior at 800 °C cannot be described by the particle growth kinetic of Eq. (7), and is therefore plotted as a dotted line in Fig. 7. A physical explanation of the observed decreasing trend can be proposed remembering that the data of Fig. 7 come from the reflection due to the [440] plane of the γ polymorph. While this is the only, or at least the dominant, one at lower and intermediate temperatures, at 800 °C it is probably the first one to nucleate and grow, but other phases also nucleate, and eventually grow also consuming the γ crystallites. Considering now only the temperatures for which the growth kinetic model is valid, it can be noticed how, at least for low dose levels, there is a satisfactory correspondence with experimental points, confirming the validity of the chosen model. At higher dpa levels, the lines begin to tangle one with the other, even though all the curves converge towards an approximate value of 15–20 nm. The kinetic growth law, previously reported, can describe the growth of a single phase in the absence of other competing phases. This could explain why each fitting curve is well shaped describing the experimental points in the first part of the RIC at low radiation levels. While they lose the describing capability at higher levels of dose.

Table 2 presents the values obtained by the best fit procedure for the exponent n and the initial particle dimensions D_0 for the γ [440] reflections.

First, although a general model to describe the temperature dependence of n does not exist, as discussed previously, we observe a linear dependence of these two quantities as shown in Fig. 9. It should be noted that the parameter n describes the particle growth speed, hence a strong temperature dependence was expected. Indeed, considering the typical relationships describing crystallization, a clear inverse dependence

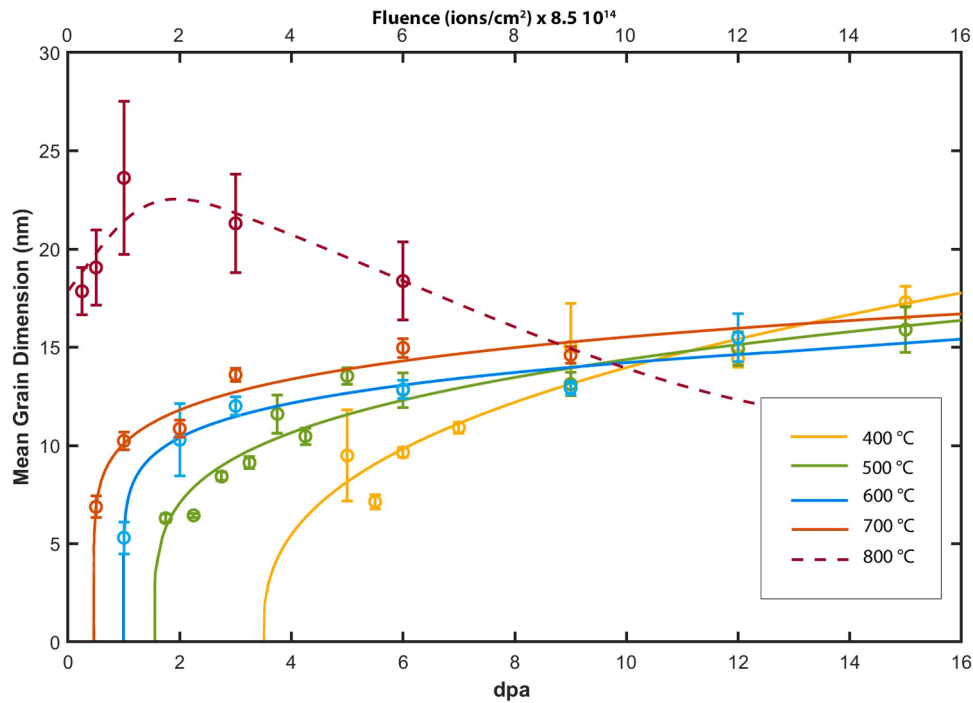


Fig. 7. Mean crystallite dimension evolution for each temperature. The model fitted using Eq. (7) is here represented by the solid lines. The 800 °C case can not be represented by the model discussed (dotted line). The data relates the 700 keV Kr^{2+} ions in the 100 nm Al_2O_3 film.

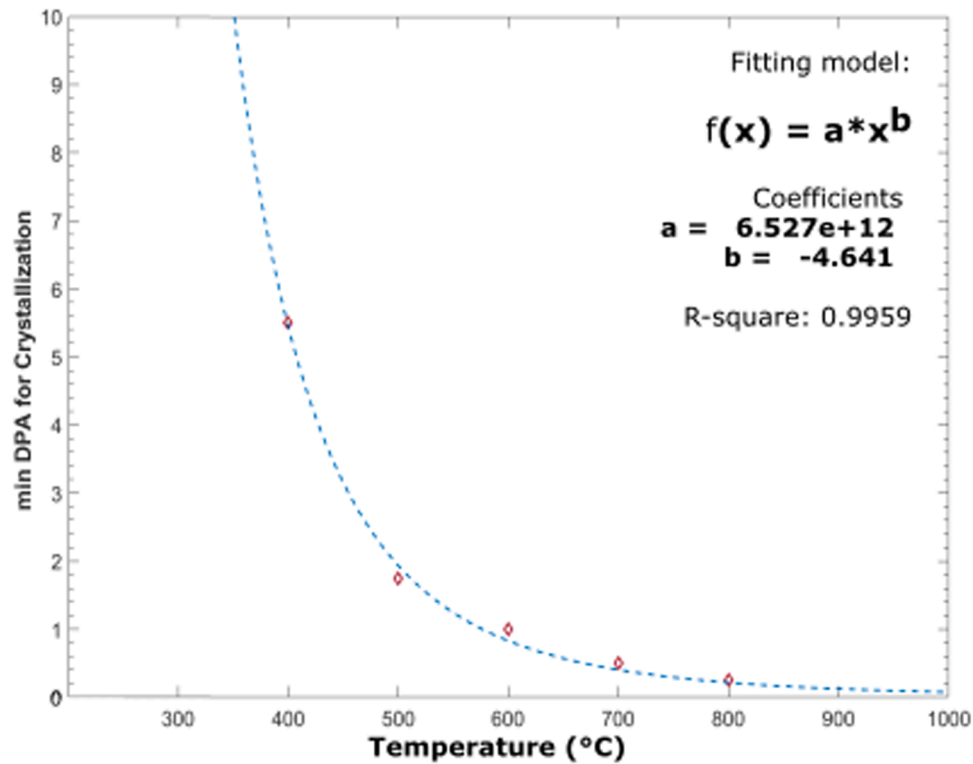


Fig. 8. Dose at which RIC is experimentally observed, for various temperatures. The trend is well described by a power law [R-square = 0.99].

between temperature and crystallization time exists [58].

The kinetic constant K has a clear Arrhenius-type dependence on temperature (Fig. 10). This allowed the calculation of the activation energy for the crystallization process. The γ [440] reflection's activation energy obtained is $E_a = 147.2$ kJ/mol (1.5 eV/particle). Interestingly, the value obtained is close to the values reported in the literature for

crystallization activation energies in other glassy ceramic materials [59–61]. The values represent the activation energies for elementary steps in the phase evolution mechanism of the system. In literature, this energy is usually called apparent activation energy because it is the value that can be found experimentally but that does not represent the real difference between the initial and final state [62,63]. A more

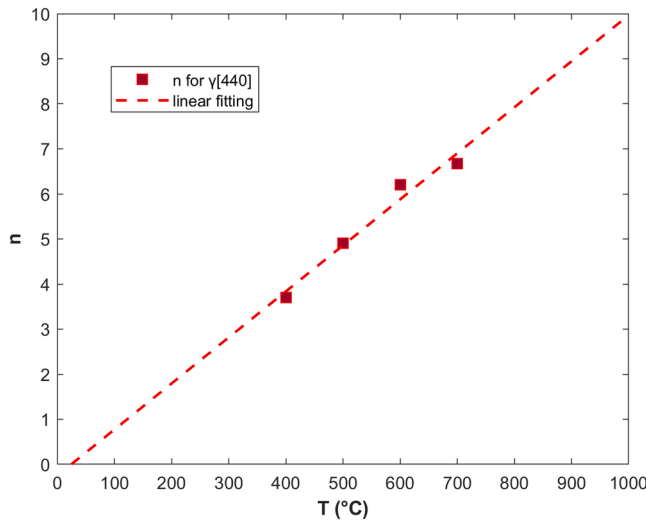
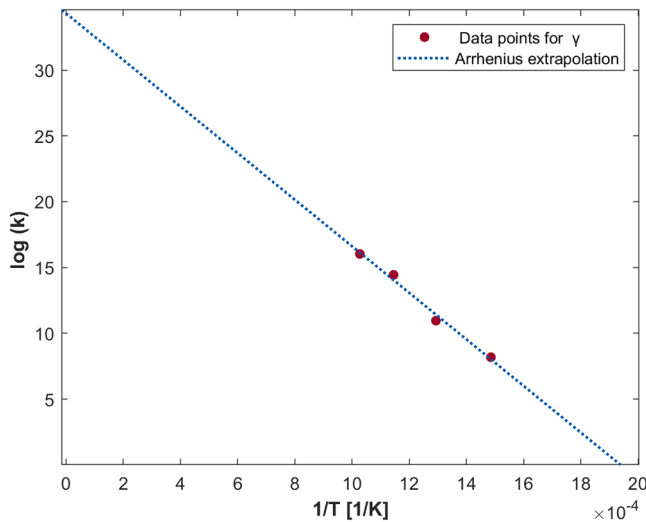
Fig. 9. Linear fitting for n .

Fig. 10. Arrhenius plots for the two different reflections analyzed.

rigorous approach should be used if the Gibbs free energies should be found. This approach is inapplicable in this case, because thermodynamic parameters such as the formation enthalpy of each step in the process [64] are unknown.

4.3. Amorphous fraction evolution

The amorphous fraction evolutions at different temperatures, obtained by the procedure discussed in Section 3.3, are reported in Fig. 11. The trends suggest the existence of an incubation dose, which decreases at increasing temperatures. Moreover, at higher temperature crystallization occurs at lower doses and causes a more pronounced decrease of the amorphous fraction. Nevertheless, it seems that a residual amorphous fraction is always present even at the highest doses and temperatures. However, the latter result shall be considered affected by a more severe uncertainty since, as discussed in Section 3.3, the identification of the amorphous fraction becomes increasingly difficult the lower it is. It is anyhow consistent with the observation of the central halo in the SAED images.

4.4. Physical mechanisms of irradiation induced nucleation and particle growth

At this point, we can speculate about mechanisms governing crystallite nucleation and subsequent particle growth observed.

The phase change phenomenon induced by electron or ion irradiation between amorphous and crystalline states has long been a complex, puzzling problem [65]. One of the most straightforward models used to explain the observed nucleation process in an amorphous system is the “thermal spike” model [65]. According to this model, a highly localized energy deposition region, the thermal spike, is created when an ion passes through the amorphous material. In this region, structural changes, chemical reactions, and the formation of nanoscale features could occur [65]. Recent molecular dynamics simulations suggest that thermal spikes could effectively be explained starting from the collision cascades produced by the ion passage. First, during each ion passage, many target’s atoms are dislodged from their lattice sites. Then, the subsequent thermal spike phase comes, in which the cascade region attains thermal equilibrium with its surrounding [66]. Moreover, the deposited energy to the electrons by slowing down the incident ions, as part of an inelastic collision, could be essential in the thermal spike creation. Indeed, the released energy diffuses within the electron subsystem by electron-electron interactions before being transferred and finally localized in the lattice system via the electron-phonon coupling [67]. This second energy transfer mode could become even more important for the irradiation process analyzed in this study, because the ENSP ratio is close to 1.0 over the film thickness (Fig. 12).

The energy deposited could ultimately lead to atomic motion and the creation of cylindrical damage along the ion path [65]. Moreover, during the thermal spike, the atoms inside the displacement cascade may reach a partially melted state (cascade melting) [66]. The combined electronic and ballistic thermal spikes associated with each ion trajectory are often used to describe and model the observed ion irradiation grain growth in ceramic polycrystalline oxides [67] and carbides and may even be used for describing the nanocrystals nucleation in amorphous materials.

Koroni et al. explained the radiation induced nucleation in amorphous material through a theoretical investigation in their paper [65]. They described the irradiation induced nucleation as a process of disordered state progressing from ordered configurations toward crystalline states by irradiation-assisted atomic rearrangement. The underlying assumption is that atomic ordering may occur as the free energy reduction of the irradiated amorphous region declines. Whether the ordered atomic configurations evolve into crystal nuclei depends on whether the crystal nuclei are more stable than the disordered situation.

Therefore, creating the thermal spike region can account for the induced nucleation observed in the alumina thin film. After the nucleation of particles occurs, the growth of the crystallites can benefit from the radiation-enhanced diffusivity. Moreover, the differences in the exponents n found and reported in Table 1 of the equations (7), compared to those found in the literature, may be attributed to the different initial matrices (polycrystalline or amorphous).

It is also worth stressing that the similarities in the phase evolution of radiation induced crystallization and thermally induced crystallization at high temperatures (Fig. 4)) may further confirm the validity of this thermal spike model.

The findings of this study are particularly intriguing with regards to the activation energy, as the conversion of 147.2 kJ/mol to 1.5 eV/particle are similar to the reported values for point defect migration energies in Al₂O₃ for both the Al-vacancy (1.8–2.1 eV/particle) and O-vacancy (1.8–2 eV/particle) [68]. This suggests a potential correlation between point defect migration and the growth of crystallite particles.

Moreover, assuming that the melting temperature of the alumina coatings is equivalent to that of the bulk crystalline alumina ($T_m \approx 2000^\circ\text{C}$ [69]), and taking into account the discussion in Kaoumi [52] regarding crystalline material, it can be inferred that the particle growth

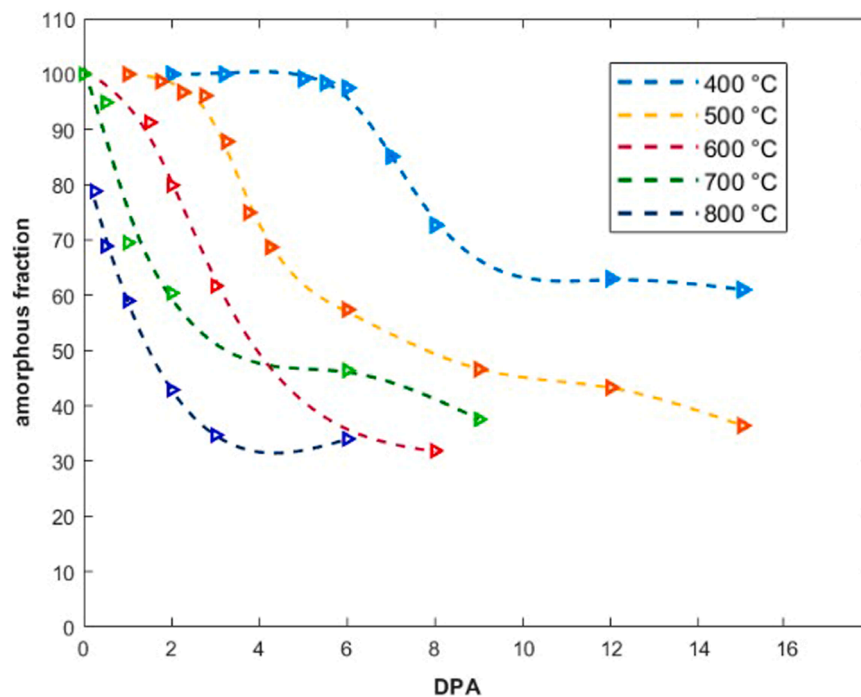


Fig. 11. The amorphous fractions at different temperatures. See the discussion in Section 3.2 of the uncertainties to be associated to the experimental data; quantitative estimates of these uncertainties cannot be given. The dashed lines, obtained by smoothing spline fitting are just a guide to the eye.

process occurs in a thermally-assisted regime (irradiation temperature above $0.15\text{--}0.20\ T_m$) where grain growth is enhanced with increasing temperature. This is precisely what was observed in this study.

All the evidence indicates that the observed processes occur in a regime where radiation can induce initial nucleation, followed by a combination of radiation-enhanced diffusion and temperature-assisted processes that facilitate further particle growth. These combined effects result in crystallization at a temperature lower than typically observed ($T < 600\ ^\circ\text{C}$).

5. Conclusions

The interplay between radiation dose and temperature on the crystallization kinetics of amorphous Al_2O_3 deposited by pulsed laser deposition was studied in depth by an in-situ study. We collected a diverse set of data across a broad temperature range ($400\text{--}800\ ^\circ\text{C}$), enabling us to develop a new semi-empirical model. We built it upon previous research on pre-existing crystallized materials, while also considering an incubation dose for radiation-induced crystallization at temperatures below the crystallization point of $\alpha\text{-Al}_2\text{O}_3$. The resulting equation effectively describes crystallization at low levels of radiation damage, whilst the discrepancy observed for higher exposures and temperature may be attributed to the formation of secondary phases. This study elucidated the existence of three distinct growth regimes and utilize a kinetic approach to determine the activation energy associated with the grain growth process. Our findings indicate a possible link between point defect migration and the nucleation of crystallite particles. Furthermore, by analyzing the intensity profiles obtained from selected area electron diffraction (SAED), we gained valuable insight into the phase evolution at various temperatures. Additionally, we investigated the evolution of the amorphous fraction at different temperatures and observed a decreasing incubation dose as the temperature increases. These results provide the first general framework to describe the complex processes involved in the structural evolution of amorphous alumina films under ion irradiation material growth and evolution, providing key information about their use as protective coatings in radiation-rich environments.

Funding sources

M.V., B.P., M.C., and F.D.F. acknowledge financial aid by the European Commission through the H2020 projects ‘GEMMA’ (Grant Agreement No. 755269) and ‘IL TROVATORE’ (GA No. 740415). This work has been carried out within the framework of the EUROfusion Consortium and has received funding from the Euratom Research and Training Programme 2014–2018 and 2019–2020 under grant agreement No 633053. The views and opinions expressed herein do not necessarily reflect those of the European Commission.

CRediT authorship contribution statement

D. Loiacono: Writing – original draft, Conceptualization, Methodology, Validation, Formal analysis, Investigation. **M. Vanazzi:** Writing – original draft, Conceptualization, Methodology, Validation, Investigation. **B. Paladino:** Investigation, Data curation. **W.-Y. Chen:** Investigation, Data curation, Methodology, Writing – review & editing. **M. Cabrioli:** Investigation, Data curation. **M. Li:** Supervision, Validation. **M.G. Beghi:** Supervision, Validation, Writing – review & editing. **F. Di Fonzo:** Supervision, Conceptualization, Funding acquisition, Methodology, Writing – review & editing.

Declaration of Competing Interest

The authors declare the following financial interests/personal relationships which may be considered as potential competing interests:

Matteo Vanazzi, Boris Paladino, Mattia Cabrioli reports financial support was provided by European Commission. D Loiacono, W.-Y., Chen, M. Li reports financial support was provided by US Department of Energy.

Data availability

Data will be made available on request.

Acknowledgments

This work was performed, in part, at the Intermediate Voltage Electron Microscope (IVEM)-Tandem Facility at the Argonne National Laboratories as part of a rapid turnaround experiment using funding provided by Nuclear Science User Facilities. The authors gratefully acknowledge use of facilities and instrumentation and the help throughout this study.

Supplementary materials

Supplementary material associated with this article can be found, in the online version, at doi:10.1016/j.jnucmat.2023.154805.

References

- [1] Lorenzo Malerba, et al., Materials for sustainable nuclear energy: a european strategic research and innovation agenda for all reactor generations, *Energies* 15 (5) (2022) issn: 1996-1073. url: <https://www.mdpi.com/1996-1073/15/5/1845>.
- [2] Marco Utili, et al., Design of the test section for the experimental validation of anti-permeation and corrosion barriers for WCLL BB, *Appl. Sci.* 12 (3) (2022) issn: 2076-3417.
- [3] F. García Ferré, et al., Advanced Al₂O₃ coatings for high temperature operation of steels in heavy liquid metals: a preliminary study, *Corros. Sci.* 77 (2013) 375–378.
- [4] F.G. Ferré, et al., Corrosion and radiation resistant nanoceramic coatings for lead fast reactors, *Corros. Sci.* 124 (2017) 80–92.
- [5] D. Iadicicco, et al., Multifunctional nanoceramic coatings for future generation nuclear systems, *Fusion Eng. Des.* 146 (2019) 1628–1632.
- [6] Ferré Francisco García, et al., The mechanical properties of a nanocrystalline Al₂O₃/a- Al₂O₃ composite coating measured by nanoindentation and Brillouin spectroscopy, *Acta Mater* 61 (7) (2013) 2662–2670.
- [7] Erkkä J. Frankberg, et al., Highly ductile amorphous oxide at room temperature and high strain rate, *Science* 366 (6467) (2019) 864–869.
- [8] Daniele Iadicicco, et al., Efficient hydrogen and deuterium permeation reduction in Al₂O₃ coatings with enhanced radiation tolerance and corrosion resistance, *Nucl. Fusion*. 58 (2018).
- [9] A. Zaborowska, et al., Absolute radiation tolerance of amorphous alumina coatings at room temperature, *Ceram. Int.* 47 (24) (2021) 34740–34750, issn: 0272-8842.
- [10] C. Abromeit, Aspects of simulation of neutron damage by ion irradiation, *J. Nucl. Mater.* 216 (1994) 78–96.
- [11] J. Sun, et al., Study of the magnetic modifications of Fe₃O₄ ferrite thin films induced by 2.03 GeV Kr ions irradiation, *Nucl. Instrum. Method. Phys. Res. Sect. B: Beam Interact. Mater. Atoms* 269 (9) (2011) 873–875.
- [12] Lionel Thomé, et al., Radiation effects in nuclear materials: role of nuclear and electronic energy losses and their synergy, in: *The 18th International Conference on Ion Beam Modifications of Materials (IBMM2012)* 307, 2013, pp. 43–48, issn: 0168-583X.
- [13] S.J. Zinkle, Effect of irradiation spectrum on the microstructure of ion-irradiated Al₂O₃, in: *MRS Symposium Proceedings* 373, 1994, pp. 287–292.
- [14] N. Khalfaoui, et al., Damage creation threshold of Al₂O₃ under swift heavy ion irradiation, *Nucl. Instrum. Method. Phys. Res. Sect. B: Beam Interact. Mater. Atoms* 286 (2012) 247–253.
- [15] Ji Miaomiao, “Computational Characterization of Radiation-Induced Defect Dynamics and Material Response”. PhD thesis, Massachusetts Institute of Technology. Department of Nuclear Science and Engineering, 2019.
- [16] Yanwen Zhang, et al., Coupled electronic and atomic effects on defect evolution in silicon carbide under ion irradiation, *Curr. Opin. Solid State Mater. Sci.* 21 (6) (2017) 285–298, issn: 1359-0286.
- [17] Lionel Thomé, et al., Combined effects of nuclear and electronic energy losses in solids irradiated with a dual-ion beam, *Appl. Phys. Lett.* 102 (14) (2013), 141906, <https://doi.org/10.1063/1.4801518>.
- [18] Lionel Thomé, et al., Behavior of nuclear materials irradiated with a dual ion beam, *Nucl. Instrum. Methods Phys. Res., Sect. B* 326 (2014), <https://doi.org/10.1016/j.nimb.2013.09.054>, 17th International Conference on Radiation Effects in Insulators (REI), pp. 219–222, issn: 0168-583X.
- [19] S.J. Zinkle, Effect of irradiation spectrum on the microstructural evolution in ceramic insulators, *J. Nucl. Mater.* 219 (1995) 113–127, [https://doi.org/10.1016/0022-3115\(94\)00662-8](https://doi.org/10.1016/0022-3115(94)00662-8). Fabrication and Properties of Ceramics for Fusion Energy, issn: 0022-3115.
- [20] F. García Ferré, et al., Radiation endurance in Al₂O₃ nanoceramics, *Sci. Rep.* 6 (2016).
- [21] F. García Ferré, et al., Extreme ion irradiation of oxide nanoceramics: influence of the irradiation spectrum, *Acta Mater.* 143 (2018) 156–165.
- [22] F. Di Fonzo, Growth regimes in pulsed laser deposition of aluminum oxide films”, *en, Appl. Phys. A* 93 (3) (2008) 765–769.
- [23] Meimei Li, Wei-Ying Chen, Peter M. Baldo, In situ transmission electron microscopy with dual ion beam irradiation and implantation, *Mater. Charact.* 173 (2021), 110905.
- [24] James F. Ziegler, M.D. Ziegler, J.P. Biersack, SRIM – The stopping and range of ions in matter (2010), *Nucl. Instrum. Methods Phys. Res., Sect. B* 268 (11) (2010) 1818–1823, 19th International Conference on Ion Beam Analysis.
- [25] Kai Nordlund, et al., Primary radiation damage: a review of current understanding and models, *J. Nucl. Mater.* 512 (2018) 450–479.
- [26] R.E. Stoller, et al., On the use of SRIM for computing radiation damage exposure, *Nucl. Instrum. Methods Phys. Res., Sect. B* 310 (2013) 75–80.
- [27] NUCLEAR ENERGY AGENCY, Primary Radiation Damage in Materials, OECD/NEA, 2015. Report.
- [28] S. Agarwal, et al., On the use of SRIM for calculating vacancy production: quick calculation and full-cascade options, *Nucl. Instrum. Methods Phys. Res., Sect. B* 503 (2021) 11–29, issn: 0168-583X, url: <https://www.sciencedirect.com/science/article/pii/S0168583X21002299>.
- [29] M.J. Norgett, M.T. Robinson, I.M. Torrens, A proposed method of calculating displacement dose rates, *Nucl. Eng. Des.* 33 (1) (1975) 50–54, [https://doi.org/10.1016/0029-5493\(75\)90035-7](https://doi.org/10.1016/0029-5493(75)90035-7), issn: 0029-5493.
- [30] P. Souza Santos, H. Souza Santos, S.P. Toledo, Standard transition aluminas. Electron microscopy studies, *Mater. Res.* 3 (2000) 104–114.
- [31] Balaraman Sathiyaseelan, Iruson Baskaran, Kandasamy Sivakumar, Phase transition behavior of nanocrystalline Al₂O₃ powders, *Soft Nanosci. Lett.* 03 (2013) 69–74.
- [32] Linus Pauling, Sterling B. Hendricks, The crystal structures of hematite and corundum, *J. Am. Chem. Soc.* 47 (3) (1925) 781–790.
- [33] Samir Lamouri, et al., Control of the γ -alumina to α -alumina phase transformation for an optimized alumina densification, *Boletín de la Sociedad Española de Cerámica y Vidrio* 56 (2) (2017) 47–54, issn: 0366-3175.
- [34] David Mitchell, DiffTools: electron diffraction software tools for DigitalMicrograph™, *Microsc. Res. Tech.* 71 (2008) 588–593.
- [35] W.S. Rasband, C.A. Schneider, K.W. Eliceiri, NIH Image to ImageJ: 25 years of image analysis, *Nat. Methods* (2012).
- [36] A.A. Othman, K. Tahon, M. Osman, Glass transition and crystallization kinetic studies in Mg_{0.10}As_{0.34}Se_{0.56} chalcogenide glass by using non-isothermal techniques, *Physica B-Condensed Matter* 311 (2002) 356–365.
- [37] D. Turnbull J.E. Burke, Recrystallization and grain growth, *Progr. Metal Phys.* 3 (1952) 220–292, issn: 0502-8205.
- [38] Corrado Spinel, Salvatore Lombardo, Francesco Priolo, Crystal grain nucleation in amorphous silicon, *J. Appl. Phys.* 84 (10) (1998) 5383–5414.
- [39] R. Nuernberg, O. Montedo, Crystallization kinetics of β -spodumene/cordierite-based glass-ceramics, *Mater. Sci. Forum* 881 (2016) 83–88.
- [40] Jaromir Moravec, Determination of the grain growth kinetics as a base parameter for numerical simulation, *deman, MM Sci. J.* (2015) 649–653.
- [41] Alan Giunelli, Auskinetics and the Grain Size Distribution, *Grain Growth, University of Wollongong*, 1991.
- [42] Peng Cao, Li Lu, M.O. Lai, Grain growth and kinetics for nanocrystalline magnesium alloy produced by mechanical alloying, *Mater. Res. Bull.* 36 (Mar. 2001).
- [43] Shu Hu, Paul C. McIntyre, Nucleation and growth kinetics during metal-induced layer exchange crystallization of Ge thin films at low temperatures, *J. Appl. Phys.* 111 (4) (2012), 044908.
- [44] S.K. Dutta, R.M. Spriggs, Grain growth in fully dense ZnO, *J. Am. Ceram. Soc.* 53 (1) (1970) 61–62.
- [45] C.M. KAPADIA, M.H. LEIPOLD, Grain growth in pure dense MgO, *J. Am. Ceram. Soc.* 57 (1) (1974) 41–42.
- [46] PETROVIC V. M.M. Ristic, Isochronal and isothermal grain growth during sintering of cadmium oxide, *Metallography* 13 (1980) 319–327.
- [47] T.Y. Tien, E.C. Subbarao, Grain growth in Ca_{0.16}Zr_{0.84}O_{1.84}, *J. Am. Ceram. Soc.* 46 (10) (1963) 489–492.
- [48] T. Spassov, U. Köster, Grain-growth in nanocrystalline zirconium-based alloys, *J. Mater. Sci.* 28 (10) (1993) 2789–2794.
- [49] G.T. Higgins, Grain-boundary migration and grain growth, *Metal Sci.* 8 (1) (1974) 143–150.
- [50] Jiang Shi, et al., Kinetic analysis of crystallization in Li₂O-Al₂O₃-SiO₂-B₂O₃-BaO glass-ceramics, *J. Non Cryst. Solids* 491 (2018) 106–113.
- [51] D. Kaoumi, Arthur Thompson Motta, R.C. Birtcher, Grain growth in nanocrystalline metal thin films under in situ ion-beam irradiation, *Effect. Radiat. Mater.* (2008) 206–218. ASTM Special Technical Publication. Effects of Radiation on Materials: 23rd International Symposium; Conference date: 13-06-2006 Through 15-06-2006. ASTM International.
- [52] D. Kaoumi, A.T. Motta, R.C. Birtcher, A thermal spike model of grain growth under irradiation, *J. Appl. Phys.* 104 (7) (2008), 073525, <https://doi.org/10.1063/1.2988142>.
- [53] Hanns Gietl, et al., Neutron irradiation-enhanced grain growth in tungsten and tungsten alloys, *J. Alloys Compd* 901 (2022), 163419, <https://doi.org/10.1016/j.jallcom.2021.163419> issn: 0925-8388.
- [54] D. Jensen, Estimation of the size distribution of spherical, disc-like or ellipsoidal particles in thin foils, *J. Phys. D: Appl. Phys.* 28 (3) (1995) 549–558.
- [55] Thomas M. Hare, John C. Russ, Jay E. Lane, Volume determination of TEM specimens containing particles or precipitates, *J. Electron. Microsc. Tech.* 10 (1) (1988) 1–6.
- [56] Alwyn Eades, Electron crystallography: electron microscopy and electron diffraction, X. Zou, S. Hovmöller, and P. Oleynikov. Oxford University Press (IUCr Texts on Crystallography 16), 2011, 335 pages. ISBN 978-0-19-958020-0 (Hardcover), *Microsc. Microanal.* 18 (3) (2012) 645–646.
- [57] M. Vanazzi, “Development of Advanced Nano-Ceramic Coatings for Future Generation Nuclear Reactors” PhD Thesis, Politecnico di Milano, 2019.
- [58] Donald R. Askeland, Wendelin J. Wright, *Sci. Eng. Mater.* (2016).
- [59] M. Ghasemzadeh, et al., Crystallization kinetics of glass-ceramics by differential thermal analysis, *Ceram. Silik.* 55 (2011) 188–194.

- [60] R.B. Nuernberg, C.A. Faller, O.R.K. Montedo, Crystallization kinetic and thermal and electrical properties of β -spodumeness/cordierite glass-ceramics, *J. Therm. Anal. Calorim.* 127 (1) (2016) 355–362.
- [61] M.I. Abd-Elrahman, et al., The activation energies at glass transition temperatures and dynamic fragility of (Se₉₀Te₁₀)_{100-x} In_x glassy alloys, *Thermochim. Acta* 672 (2019) 86–92.
- [62] Ioannis Nikolakakis, Kyriakos Kachrimanis, Crystallization kinetics of orthorhombic paracetamol from supercooled melts studied by non-isothermal DSC, *Drug. Dev. Ind. Pharm.* 43 (2017) 257–263.
- [63] Siuli Dutta, et al., Microstructural evolution, recovery and recrystallization kinetics of isothermally annealed ultra low carbon steel, *Mater. Res. Express* 7 (Jan. 2020).
- [64] Zhongtian Mao, Charles T. Campbell, Apparent activation energies in complex reaction mechanisms: a simple relationship via degrees of rate control, *ACS Catal* 9 (10) (2019) 9465–9473.
- [65] Cyrus Koroni, et al., Irradiation-induced amorphous-to-crystalline phase transformations in ceramic materials, *Materials (Basel)* 15 (17) (2022), <https://doi.org/10.3390/ma15175924> issn: 1996-1944.
- [66] A. Meldrum, et al., A transient liquid-like phase in the displacement cascades of zircon, Hafnon and Thorite, *Nature* 395 (1998) 56–58, <https://doi.org/10.1038/25698>.
- [67] Marcel Toulemonde, E. Paumier, Christian Dufour, Thermal spike model in the electronic stopping power regime, *Radiat. Eff. Defects Solids* 126 (Mar. 1993) 201–206, <https://doi.org/10.1080/10420159308219709>.
- [68] S.J. Zinkle, C. Kinoshita, Defect production in ceramics, *J. Nucl. Mater.* 251 (1997) 200–217, [https://doi.org/10.1016/S0022-3115\(97\)00224-9](https://doi.org/10.1016/S0022-3115(97)00224-9). Proceedings of the International Workshop on Defect Production, Accumulation and Materials Performance in an Irradiation Environment issn: 0022-3115.
- [69] R.F. Geller, Paul J. Yavorsky, Melting point of alpha-alumina, *J. Res. Natl. Bur. Stand.* (1934) 34 (1945) 395.